

A unified steady and unsteady formulation for hydrodynamic potential flow simulations with fully nonlinear free surface boundary conditions

Andrea Mola*, Nicola Giuliani†, Óscar Crego‡, Gianluigi Rozza§

October 7, 2022

Abstract

This work discusses the correct modeling of the fully nonlinear free surface boundary conditions to be prescribed in water waves flow simulations based on potential flow theory. The main goal of such a discussion is that of identifying a mathematical formulation and a numerical treatment that can be used both to carry out transient simulations, and to compute steady solutions — for any flow admitting them. In the literature on numerical towing tank in fact, steady and unsteady fully nonlinear potential flow solvers are characterized by different mathematical formulations. The kinematic and dynamic fully nonlinear free surface boundary conditions are discussed, and in particular it is proven that the kinematic free surface boundary condition, written in semi-Lagrangian form, can be substituted by an equivalent non penetration boundary condition by all means identical to the one used on the surface of floating bodies or on the basin bottom. The simplified mathematical problem obtained is discretized over space and time via Boundary Element Method (BEM) and Implicit Backward Difference Formula (BDF) scheme, respectively. The results confirm that the solver implemented is able to solve steady potential flow problems just by eliminating null time derivatives in the unsteady formulation. Numerical results obtained confirm that the solver implemented is able to accurately reproduce results of classical steady flow solvers available in the literature.

*Scuola IMT Alti Studi Lucca, Piazza S. Ponziano, 6 - 55100 Lucca, Italy, andrea.mola@imtlucca.it

†previously Scuola Internazionale Superiore di Studi Avanzati (SISSA), now Applied Materials Inc., Santa Clara, CA 95054-3299 USA, nicola.giuliani@amat.com

‡Departamento de Matemática Aplicada, Universidade de Santiago de Compostela, Santiago de Compostela E-15782, Spain. oscar.crego@usc.es

§Scuola Internazionale Superiore di Studi Avanzati (SISSA) via Bonomea, 265 - 34136 Trieste, Italy, grozza@sissa.it

Contents

1	Introduction	2
2	Fluid dynamic model based on potential flow theory	6
2.1	Governing equations	6
2.2	Free surface boundary conditions	9
2.2.1	Derivation of Lagrangian free surface boundary conditions	9
2.2.2	Semi-Lagrangian (or Arbitrary Lagrangian–Eulerian) free surface boundary conditions	11
2.2.3	Equivalent kinematic free surface boundary condition formulation	12
2.3	The final boundary value problem	13
3	Boundary value problem discretization	14
3.1	Laplace equation discretization based on Boundary Element Method	15
3.1.1	Boundary integral formulation	16
3.1.2	Discretisation	16
3.1.3	Numerical Implementation	18
3.2	Dynamic free surface boundary condition spatial discretization	18
3.3	Time advancing scheme	20
3.4	DAE restart procedure	20
3.5	Stationary solver	21
4	Results	22
4.1	The immersed ellipsoid test case description	22
4.1.1	Steady state numerical experiments	23
4.1.2	Unsteady numerical experiments	24
4.2	Numerical results	26
4.2.1	Steady case results	27
4.2.2	Unsteady case results	33
5	Conclusions and future perspectives	35
6	Acknowledgments	36

1 Introduction

The progress witnessed in the last decades has established computational tools for fluid dynamic performance prediction as a reliable instrument available to boat and ship designers, and a valid alternative to the experimental

approach. Along with a steady increase in computational power and resources, such progress has to be ascribed to the constant improvement of mathematical models and numerical algorithms. Among the many methods developed in the effort to obtain fast and yet accurate hydrodynamic simulations, potential flow models complemented by fully nonlinear free surface boundary conditions have enjoyed considerable success in the naval architecture community. In fact both the incompressible fluid and irrotational flow assumptions upon which the potential flow theory is based appear quite reasonable for slender hulls advancing at moderate cruise speeds. In addition, compared to their linearized free surface boundary condition counterparts, fully nonlinear potential models enjoy superior accuracy, which makes them able to predict displacement hulls resistance with errors as low as 2% and water elevations within experimental uncertainty ([29]). On the other hand, compared to more general models based on Navier–Stokes equations, such as RANS or LES, they clearly lead to smaller discretized problems and to faster computations. Several potential flow models are available in the literature for solving steady nonlinear free surface flows past a ship hull. Among others, we mention the work of Raven [34], which resulted in the implementation of the commercial software RAPID, and of Janson [20, 21], which led to the commercial code SHIPFLOW. Over the years, these steady state solvers have established themselves as fast and reliable tools for the early design stages, in which they can provide not only ship wave resistance estimates, but also pressure distributions, free surface elevation and velocity fields surrounding the hull.

As opposed to the steady case, the extension of such fully nonlinear potential algorithms to the unsteady case has instead proved to be a nontrivial task. As a consequence, the examples of successful numerical towing tank solvers implementing the unsteady potential model with nonlinear free surface boundary conditions are less abundant. The most common approach for unsteady free surface potential flow simulations (see, e.g., Grilli et al. [15]) is the mixed Eulerian–Lagrangian approach (MEL) originally introduced by Longuet-Higgins and Cokelet [26]. In such a framework, at each time step the Laplace equation problem for the fluid velocity potential is solved in the Eulerian step, and the resulting fluid velocity field is then used to compute, in a Lagrangian step, the time evolution of the free surface position and potential to be used at the next time step. In the MEL formulation, the fluid dynamic grid nodes follow the fluid particles on the free surface in a Lagrangian fashion, which in presence of a stream flowing past a ship hull, requires periodic regridding, which increases the computational cost and the implementation complexity of the algorithm (ee, e.g., Kjellberg et al. [24], and Kjellberg [23]). This problem is in principle avoided using a semi-Lagrangian formulation of the free surface boundary conditions, as originally suggested in by Beck [5]. The time derivatives appearing in Beck boundary conditions equations are neither computed on fixed spatial points

as in the Eulerian formulation, nor on fixed fluid particles as in the Lagrangian formulation. Instead, they are computed on fixed grid nodes — or free surface markers —, which move with a prescribed velocity field. Such a formulation, by all means similar to what in other contexts is referred to as Arbitrary Lagrangian–Eulerian (or ALE, [9]), allows for the resolution of the nonlinear free surface problem using a time advancing identical to the one used in MEL, and in principle it does not require regridding. However, a saw-tooth instability arising from dominant transport terms appearing in the boundary conditions, make semi-Lagrangian unstable whenever the grid and fluid velocity difference is non negligible. For such a reason, the methodology combining semi-Lagrangian and MEL could only be used in ([37]) by setting a grid stream velocity equal to the fluid one, which only mitigates the regridding problem. Or, as an alternative, no stream It was not until a decade ago (see [30, 14]) that a proper stabilization mechanism was introduced to allow for stable simulations based on semi-Lagrangian boundary conditions, at all nonplaning boat speeds and with no remeshing required on unstructured and adaptively refined grids. Moreover, [30] presents a novel time advancing approach in which the spatially discretized equations of the govern boundary value problem are treated as a Differential Algebraic Equation (DAE) system, in which the algebraic components result from the Laplace equation discretization and the differential components result from the spatial integration of the time dependent free surface boundary conditions. The DAE is finally solved by means of an implicit Backward Differentiation Formula.

The recount just presented shows how different the path towards accurate and robust flow simulations was for transient potential flow model with fully nonlinear free surface boundary conditions, with respect to its steady counterpart. As a consequence of this not only distinct algorithms have been developed to carry out steady or unsteady simulations, but also different govern equations are used. Indeed, the steady solver fully nonlinear free surface boundary treatment is significantly different from the transient model one. The former solvers are in fact based on a single boundary condition combining the kinematic and dynamic conditions ([38, 34, 20, 21]) found in the unsteady formulation. As noted by Raven in the introduction of his PhD dissertation ([34],page 67), a unified approach for steady and transient fully nonlinear potential flow simulations, was missing at the time. And, to the best of the authors knowledge, it is missing to this day. This fact represents a clear anomaly with respect to other fluid dynamic or more in general continuum mechanics models. In such dynamical systems in fact, the steady solution is typically sought simply through elimination of the time derivatives from the unsteady govern equations. However, it is clear that the only frame of reference in which steady flow can be observed, is that of a hull advancing in calm water. For this reason, all the models based on MEL and Lagrangian free surface boundary conditions ([23],

[15]), cannot lead to a steady solution, since in presence of a steady stream velocity the free surface particle positions never settle for an equilibrium position. The same can be said for all the transient methods that, to avoid instabilities, employ a combination of MEL and semi-Lagrangian free surface conditions with a grid stream velocity ([37]). On the other hand, the stabilized semi-Lagrangian free surface model presented in ([30]), presents no average grid stream velocity and can in principle be used to obtain a solver that is switched from unsteady to steady by only removing the time derivatives from the govern equations.

In this work, we present all the modifications to the stabilized semi-Lagrangian free surface model presented in ([30]), so that it can be successfully used both as a steady and unsteady solver. As will be discussed, further modifications are made to the transient free surface model, to make it also compatible with steady state solution. In particular, the semi-Lagrangian kinematic free surface boundary condition is substituted by a non homogeneous Neumann boundary condition, written in ALE formulation. Such a condition is substantially a non penetration constraint for the fluid on the moving boundary, and is identical to the conditions imposed on other non penetration regions such as the hull or bottom boundaries. The presence in the system of the dynamic semi-Lagrangian free surface boundary condition allows for the simultaneous computation of the free surface grid velocity, which is the additional unknown of the problem. A proof will be offered that the non penetration Neumann boundary condition is equivalent to the semi-Lagrangian kinematic free surface condition on the free surface. Several numerical experiments will then show that the transient solver can be used to obtain steady solution just “turning off” all time derivatives in the govern equations. In addition, to confirm that the present approach recovers the results of classic steady solvers, the steady state results will be compared to results on the same test cases obtained by Scullen ([38]).

The content of this paper is organized as follows. Section 2 introduces the equations of the model for the free surface flow, based on the potential flow theory. Details of the free surface modeling will be also presented in such section. Section 3 describes the numerical discretization of the problem based on a combined Boundary Element Method (BEM) and Finite Element Method (FEM) approach, with implicit Backward Difference Formula (BDF) time advancing scheme. Section 4 provides a description of the numerical test cases considered, and of the results obtained. Finally, Section 5 reports some brief conclusion remarks, and possible follow up investigations.

2 Fluid dynamic model based on potential flow theory

As mentioned, the main goal of this work that of identifying a unified mathematical model to carry out both steady and unsteady simulations of the potential flow past a body advancing at constant speed in calm water. We point out that by *steady flow* we indicate a flow in which all the Eulerian derivatives of the pressure field and velocity field are null, namely

$$\frac{\partial p(\mathbf{x}, t)}{\partial t} = 0 \quad \frac{\partial \mathbf{u}(\mathbf{x}, t)}{\partial t} = 0. \quad (1)$$

In such conditions we have that the flow fields $p(\mathbf{x}, t) = p(\mathbf{x})$ and $\mathbf{u}(\mathbf{x}, t) = \mathbf{u}(\mathbf{x})$ are only dependent on the point position vector $\mathbf{x} = x\mathbf{e}_x + y\mathbf{e}_y + z\mathbf{e}_z$. Purely kinematic considerations suggest that whenever the flow is driven by the motion of a body within an initially still mass of fluid, the only frame of reference in which a steady state solution can be observed is a body attached frame. Of course, there are situations in which even in a body attached reference frame a steady state is not possible. This is for instance the case of the flow past an accelerating body. In all those situations, resorting to an unsteady formulation will be mandatory. In the present section we will start discussing the latter, more general case, and successively consider its steady variant.

2.1 Governing equations

The flow domain $\Omega(t)$, $\forall t \geq 0$ is the simply connected and time dependent three dimensional region occupied by water, surrounding and following the body. In such a region — depicted in Figure 1, along with its boundaries — assuming irrotational flow, the velocity field admits a scalar potential $\Phi(\mathbf{x}, t)$, namely

$$\mathbf{u}(\mathbf{x}, t) = \nabla \Phi(\mathbf{x}, t) = \mathbf{U}_\infty(t) \cdot \mathbf{x} + \phi(\mathbf{x}, t) \quad \forall \mathbf{x} = x\mathbf{e}_x + y\mathbf{e}_y + z\mathbf{e}_z \in \Omega(t) \subseteq \mathbb{R}^3 \quad (2)$$

where $\phi(\mathbf{x}, t)$ is the perturbation potential and $\mathbf{U}_\infty(t)$ is the asymptotic velocity vector, corresponding to the apparent water stream velocity in the moving reference frame of the surging body.

The equations of motion that describe the velocity and pressure fields $\mathbf{u}(\mathbf{x}, t)$ and $p(\mathbf{x}, t)$ in the fluid region surrounding the moving body are the incompressible Navier–Stokes equations. For a detailed derivation potential flow equations applied to nonlinear water wave, and the corresponding

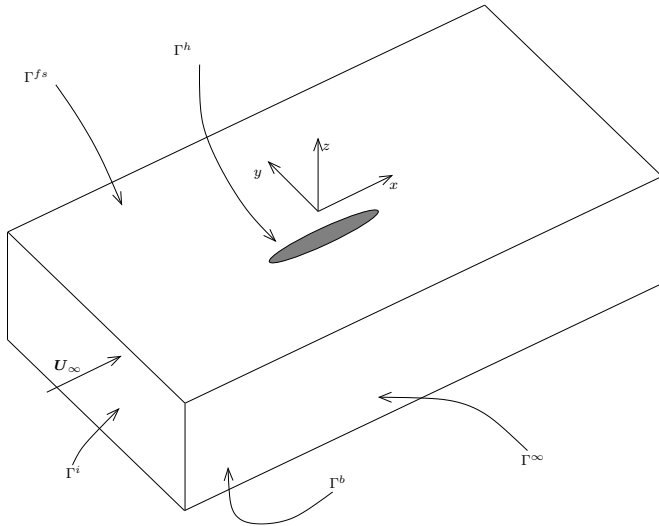


Figure 1: A sketch of the computational domain $\Omega(t)$. The diagram also shows the location of the body, free surface, bottom, inflow and far field boundary regions Γ^h , Γ^{fs} , Γ^b , Γ^i and Γ^∞ , respectively. The stream velocity \mathbf{U}_∞ also indicates that $\Omega(t)$ is located in a hull attached frame, and follows the body in its motions.

boundary value problem, we refer the interested readers to [30]. In the present discussion, we will report the main results, with focus on aspects that are relevant to obtaining a well posed boundary value problem that remains well posed in presence of steady flow. Under the aforementioned assumptions, the continuity and momentum equation can be recast into the Laplace Equation for the velocity potential and the unsteady Bernoulli equation, respectively. We have

$$\Delta\phi = 0 \quad \text{in } \Omega(t), \forall t \geq 0 \quad (3)$$

$$\frac{\partial\phi}{\partial t} + \frac{1}{2}|\mathbf{U}_\infty + \nabla\phi|^2 + \mathbf{g} \cdot \mathbf{x} + \frac{p}{\rho} = C(t) \quad \text{in } \Omega(t), \forall t \geq 0. \quad (4)$$

Here, ρ indicates the — constant — density of the fluid and the reference frame gravity acceleration vector \mathbf{g} is used in the corresponding gravity forces potential term. In particular, in the case of inertial reference frame, $\mathbf{g} = g\mathbf{e}_z$, where $g = 9.81 \text{ m/s}^2$ is the earth gravity acceleration. Since pressure only appears in Equation (4), a typical approach in potential flow theory is that of solving Equation (3) to obtain the perturbation potential, which is then introduced in Bernoulli's equation to evaluate the pressure field. Thus, our govern equation is the Laplace equation for the perturbation potential field, from which both velocity and pressure fields can be recovered by means of Equations (2) and (4), respectively. To obtain a well posed problem for the perturbation potential field, the Laplace equation must be complemented

by a suitable set of conditions on the domain boundary $\partial\Omega(t) = \Gamma(t) = \Gamma^b \cup \Gamma^h \cup \Gamma^f(t) \cup \Gamma^i \cup \Gamma^\infty$, $\forall t \geq 0$. We consider the free surface $\Gamma^f(t)$ the only part of the boundary not fixed, we will drop the explicit dependence on time for the sake of simplicity. On the bottom boundary Γ^b of the basin we set a non penetration boundary condition, namely

$$\mathbf{u}(\mathbf{x}, t) \cdot \mathbf{n} = (\mathbf{U}_\infty(t) + \nabla\phi(\mathbf{x}, t)) \cdot \mathbf{n} = 0 \quad \text{on } \Gamma^b. \quad (5)$$

Assuming that Γ^b position is fixed and its orientation is horizontal, the asymptotic velocity is also horizontal and perpendicular to the boundary outward normal vector \mathbf{n} . This results in the following homogeneous Neumann boundary condition

$$\frac{\partial\phi(\mathbf{x}, t)}{\partial n} = \nabla\phi(\mathbf{x}, t) \cdot \mathbf{n} = 0 \quad \text{on } \Gamma^b. \quad (6)$$

A non penetration boundary condition is also used on the body surface Γ^h . In this case, no assumptions on the relative orientation of $\mathbf{U}_\infty(t)$ and \mathbf{n} can be made. Thus, the non homogeneous Neumann body boundary condition reads

$$\frac{\partial\phi(\mathbf{x}, t)}{\partial n} = \nabla\phi(\mathbf{x}, t) \cdot \mathbf{n} = -\mathbf{U}_\infty(t) \cdot \mathbf{n} \quad \text{on } \Gamma^h. \quad (7)$$

In this work, we will make use of a homogeneous Dirichlet boundary condition on the inflow boundary Γ^i of the domain, namely

$$\phi(\mathbf{x}, t) = 0 \quad \text{on } \Gamma^i. \quad (8)$$

A further boundary condition is to be applied on the far field truncation boundary Γ^∞ of the numerical domain. Ideally, such condition should be able to translate the fact that the perturbation potential must fade to zero at great distance from the body causing the perturbation. At the same time, the boundary condition should be neutral to water waves reaching the boundary, avoiding their reflection into the basin. Given the dispersive nature of water gravity waves reaching the outer boundary of the domain, devising a wave absorbing boundary condition working effectively across a wide range of wavelengths is a rather difficult task, especially in three dimensions. For such a reason, there has been wide debate over the most effective form of the boundary condition to be applied at the far field truncation boundary of the numerical domain, and many investigations have been carried out on the subject (see for instance [8]). Discussing the strengths and weaknesses of each approach presented in the literature is clearly beyond the scope of this work, in which we have made use of a simple homogeneous Neumann boundary condition, namely

$$\frac{\partial\phi(\mathbf{x}, t)}{\partial n} = \nabla\phi(\mathbf{x}, t) \cdot \mathbf{n} = 0 \quad \text{on } \Gamma^\infty. \quad (9)$$

As such condition does not address the problem of waves reflection, it has been complemented by the presence of a numerical damping zone — or *numerical beach* — located immediately before the downstream boundary of the domain. Such damping zone was originally presented in [8], while for a more comprehensive treatment of its application to the current mathematical setup we again refer the reader to [30].

Finally, the correct conditions to be applied on the free surface boundary Γ^w to allow for an accurate tracking of the water waves are one of the most interesting and delicate modeling aspects of the application of potential flow theory to this kind of flows. In the next section, we will detail several possible choices, and discuss their implications on the well-posedness of the mathematical problem on both steady and unsteady assumptions.

2.2 Free surface boundary conditions

The first thing to be pointed out about the free surface boundary Γ^w is that its shape and position are unknown *a priori*. For such a reason, the discussion on the correct treatment of Γ^w must not only address the problem of finding the most suitable conditions for the perturbation potential ϕ , but also the correct way to update the free surface position over time. In this regard, we first focus or attention on the govern equation for the free surface position and shape. We start assuming that the water free surface elevation field η is a single valued function of the horizontal coordinates x and y , namely

$$z = \eta(x, y, t) \quad \text{on } \Gamma^f. \quad (10)$$

It is quite clear that such an assumption limits the applicability of this model to cases in which no wave breaking occurs. However, wave overturning might not only result in free surface making contact with itself, but also in the presence of vortical flow regions. Thus, we must remark that considering the presence of breaking waves might not just require a model devoid of assumption (10), it would rather require abandoning the potential flow model altogether. The development of a multi-model solver in which the potential flow equations are interfaced with viscous models in the regions in which the flow is vortical is definitely an extremely interesting research area. Yet, it again falls far beyond the scope of the present work, which instead aims at obtaining a free surface potential flow model which is efficient and robust enough to be possibly interfaced with other models.

2.2.1 Derivation of Lagrangian free surface boundary conditions

So, the knowledge of the free surface elevation field $\eta(x, y, t)$ results in the complete description of the domain shape $\Omega(t)$. $\eta(x, y, t)$ will then become one of the unknowns of the mathematical problem at hand. To write an

evolution equation for such a new variable, we move from assumption (10) to obtain a constraint $\mathcal{G}(x, y, z, t)$ which reads

$$\Gamma^f(t) = \{x \in \partial\Omega(t) : \mathcal{G}(x, t) = z - \eta(x, y, t) = 0\} \quad \forall t \geq 0. \quad (11)$$

Taking the Lagrangian derivative of $\mathcal{G}(x, y, z, t)$ we obtain

$$\frac{D\mathcal{G}}{Dt} = \frac{Dz}{Dt} - \frac{D\eta}{Dt} = 0 \quad \text{on } \Gamma^f, \quad (12)$$

which results in

$$\frac{D\eta}{Dt} = \mathbf{U}_\infty \cdot \mathbf{e}_z + \frac{\partial\phi}{\partial z} \quad \text{on } \Gamma^f. \quad (13)$$

Equation (13) is referred to as the Lagrangian form of the fully nonlinear free surface *kinematic* boundary condition. A similar boundary condition, used to update the free surface values of the perturbation potential ϕ , is obtained from the manipulation of Bernoulli equation

$$\frac{\partial\phi}{\partial t} + |\mathbf{U}_\infty + \nabla\phi|^2 + \mathbf{g} \cdot \mathbf{x} + \frac{p_a}{\rho} = C(t) + \frac{1}{2}|\mathbf{U}_\infty + \nabla\phi|^2 \quad \text{on } \Gamma^f, \quad (14)$$

which results in

$$\frac{D\phi}{Dt} = C(t) - \mathbf{g} \cdot \mathbf{x} + \frac{p_a}{\rho} + \frac{1}{2}|\mathbf{U}_\infty + \nabla\phi|^2 \quad \text{on } \Gamma^f. \quad (15)$$

We now assume that the atmospheric pressure p_a exerted by air on the water free surface is a constant and uniform field, and that its value — which is defined up to a constant — is set to zero. The assumption that the air pressure on water is a uniform field is a rather reasonable one, especially in presence of streamlined displacement vessels traveling at moderate speeds. In addition, since the perturbation potential is assumed to fade for $|\mathbf{x}| \rightarrow \infty$, and consequently the free surface elevation $\eta \rightarrow \infty$ far from the hull, it is possible to compute that $C(t) = \frac{1}{2}|\mathbf{U}_\infty|^2$. Thus, the final form of the fully nonlinear *dynamic* free surface boundary condition for the perturbation potential reads

$$\frac{D\phi}{Dt} = \frac{1}{2}|\mathbf{U}_\infty + \nabla\phi|^2 + \frac{1}{2}|\mathbf{U}_\infty|^2 - \mathbf{g} \cdot \mathbf{x} \quad \text{on } \Gamma^f. \quad (16)$$

The combined enforcement of Equations (13) and (16) on the free surface portion of the boundary Γ^f , effectively closes the mathematical problem, and allows for the solution of a well posed boundary value problem [15].

2.2.2 Semi-Lagrangian (or Arbitrary Lagrangian–Eulerian) free surface boundary conditions

However, in the framework of our analysis aimed at identifying possible stationary solutions, the Lagrangian form of the kinematic and dynamic boundary condition is not completely satisfactory. In fact, integrating Equation (13) to compute the time evolution of the coordinates of a point on Γ^f in the boat attached frame used in this work, would not result in a stationary solution. The Lagrangian nature of Equations (13) and (13), means that they are designed to follow material particles, which never really settle for an equilibrium position but instead drift around and eventually away from the surging body. Considering instead the alternative of resorting to the Eulerian form of the fully nonlinear free surface boundary conditions, also results in an unsatisfactory result. In fact, Eulerian derivatives are not suited with the presence of a domain with moving boundaries and moving meshes. As suggested by several references ([9, 10, 33]) on fluid dynamic applications of the Finite Element Method (FEM) in deforming domains, the problem related to time derivatives in the fully nonlinear boundary conditions can be solved resorting to the Arbitrary Lagrangian Eulerian (ALE) formulation. Introducing an arbitrary grid velocity field $\mathbf{v}(\mathbf{x}) : \mathbb{R}^3 \rightarrow \mathbb{R}^3$ allows for the definition of the following total derivative

$$\frac{\delta}{\delta t} = \frac{\partial}{\partial t} + \mathbf{v} \cdot \nabla . \quad (17)$$

We remark that derivative $\frac{\delta}{\delta t}$ represents the time derivative of the desired scalar field, computed following points moving according to the prescribed — grid — velocity field. Adding the term $\mathbf{v} \cdot \nabla \eta$ on both sides of Equation (13) results in

$$\frac{D\eta}{Dt} + \mathbf{v} \cdot \nabla \eta = \frac{\partial \eta}{\partial t} + (\mathbf{U}_\infty + \nabla \phi) \cdot \nabla \eta + \mathbf{v} \cdot \nabla \eta = \mathbf{U}_\infty \cdot \mathbf{e}_z + \frac{\partial \phi}{\partial z} + \mathbf{v} \cdot \nabla \eta \quad \text{on } \Gamma^f. \quad (18)$$

Rearranging the terms leads to

$$\frac{\delta \eta}{\delta t} = \mathbf{U}_\infty \cdot \mathbf{e}_z + \frac{\partial \phi}{\partial z} + (\mathbf{v} - \mathbf{U}_\infty - \nabla \phi) \cdot \nabla \eta \quad \text{on } \Gamma^f. \quad (19)$$

With a similar treatment, Equation (16) becomes

$$\frac{\delta \phi}{\delta t} = \frac{1}{2} |\mathbf{U}_\infty + \nabla \phi|^2 + \frac{1}{2} |\mathbf{U}_\infty|^2 - \mathbf{g} \cdot \mathbf{x} + (\mathbf{v} - \mathbf{U}_\infty - \nabla \phi) \cdot \nabla \eta \quad \text{on } \Gamma^f. \quad (20)$$

Equations (19) and (20) are the ALE formulation of the Kinematic and Dynamic fully nonlinear free surface boundary conditions. In the naval engineering literature they are typically referred to as fully nonlinear free

surface boundary conditions written in semi-Lagrangian form. They have been first introduced by Beck in [5], which pointed out that velocity field \mathbf{v} can be selected so as to avoid the downstream motion of the nodes. In particular choosing

$$\mathbf{v} = v_x \mathbf{e}_x + v_y \mathbf{e}_y + \frac{\delta \eta}{\delta t} \mathbf{e}_z \quad (21)$$

allows for the computation of the vertical velocity $\frac{\delta \eta}{\delta t}$ required to keep on the free surface a point moving with arbitrary horizontal velocities v_x and v_y . The potential flow model employing the ALE formulation of the fully nonlinear free surface boundary conditions reported in Equations (19) and (20) has been successfully implemented in several contributions ([37, 24, 30]. Its main advantage with respect to the model characterized by the Lagrangian boundary conditions, is that the arbitrary grid velocity components v_x and v_y can be selected so as to retain mesh quality. On the other hand, an inspection of the ALE boundary conditions suggests that an additional transport term appears both in Equation (13) and (16). Whenever the grid velocity \mathbf{v} becomes significantly different with respect to the fluid velocity $\mathbf{U}_\infty + \nabla \phi$, such a transport term can become dominant, leading to possible stability issues in the problem discretization. Since keeping v_x and v_y values close to 0, even in presence of high stream velocity, is necessary to avoid the downstream drift of the grid nodes, a specific stabilization method will be needed to fully exploit the advantages of the ALE formulation, as discussed in Section 3.2.

2.2.3 Equivalent kinematic free surface boundary condition formulation

It is quite interesting to point out that, by a physical standpoint, the fully nonlinear kinematic free surface boundary condition in Equation (13) represents the requirement that a material point on the free surface will remain on the free surface, which indeed is a stream surface for the fluid velocity field. In fact, the equations states that the Lagrangian time derivative of the coordinates of any point on the free surface, is equal to the local Eulerian velocity. Clearly, this consideration applies to the semi-Lagrangian boundary condition in Equation (13) too, as it is derived by its Lagrangian counterpart. So, since the free surface is a stream surface for the velocity field, intuition suggests that a simple non penetration boundary condition can be applied on such a boundary portion, rather than Equations (13) and (19). Indeed, it is possible to prove that the semi-Lagrangian formulation is equivalent to a non penetration boundary condition. To this end, we start considering the free surface tangent plane equation. At a generic point \mathbf{x} , in which the free surface normal is $\mathbf{n} = n_x \mathbf{e}_x + n_y \mathbf{e}_y + n_z \mathbf{e}_z$, the implicit equation of the tangent plane reads

$$n_x x + n_y y + n_z z = c \quad (22)$$

from which we can obtain the Cartesian equation along direction z

$$z = -\frac{n_x}{n_z}x - \frac{n_y}{n_z}y + \frac{c}{n_z}. \quad (23)$$

By its very definition, the first order derivative of the tangent plane at point \mathbf{x} coincides with that of the free surface at the same point, which gives us a simple way to compute the free surface elevation gradient as

$$\nabla \eta = -\frac{n_x}{n_z} \mathbf{e}_x - \frac{n_y}{n_z} \mathbf{e}_y. \quad (24)$$

Substituting the latter gradient representation in Equation (19), we have

$$n_z \frac{\delta \eta}{\delta t} = n_z \mathbf{U}_\infty \cdot \mathbf{e}_z + n_z \frac{\partial \phi}{\partial z} - n_x \mathbf{v}_x - n_y \mathbf{v}_y + n_y \mathbf{U}_\infty \cdot \mathbf{e}_y + n_x \frac{\partial \phi}{\partial x} + n_y \frac{\partial \phi}{\partial y} \quad \text{on } \Gamma^f. \quad (25)$$

Rearranging terms and making use of Equation (21) we obtain

$$\mathbf{v} \cdot \mathbf{n} = (\nabla \phi + \mathbf{U}_\infty) \cdot \mathbf{n} \quad \text{on } \Gamma^f, \quad (26)$$

which is the non penetration boundary condition for the perturbation potential in presence of a moving boundary. In facts, it states that the normal component of the fluid velocity must be equal to the normal component of the local boundary velocity. For our purposes, Equation (26) can be finally recast in the form of the following non homogeneous Neumann boundary condition

$$\frac{\partial \phi}{\partial n} = \nabla \phi \cdot \mathbf{n} = (\mathbf{v} - \mathbf{U}_\infty) \cdot \mathbf{n} \quad \text{on } \Gamma^f. \quad (27)$$

2.3 The final boundary value problem

So, after introducing the govern equation along with the boundary conditions, here is the complete boundary value problem considered in the present work

$$\left\{ \begin{array}{ll} \Delta\phi = 0 & \text{in } \Omega(t), \forall t \geq 0 \\ \frac{\partial\phi}{\partial n} = (\mathbf{v} - \mathbf{U}_\infty) \cdot \mathbf{n} & \text{on } \Gamma^b \cup \Gamma^h \cup \Gamma^f(t), \forall t \geq 0 \\ \frac{\partial\phi}{\partial n} = 0 & \text{on } \Gamma^\infty, \forall t \geq 0 \\ \phi = 0 & \text{on } \Gamma^i, \forall t \geq 0 \\ \frac{\delta\phi}{\delta t} = \frac{1}{2}|\mathbf{U}_\infty + \nabla\phi|^2 + \frac{1}{2}|\mathbf{U}_\infty|^2 - \\ & \mathbf{g} \cdot \mathbf{x} + (\mathbf{v} - \mathbf{U}_\infty - \nabla\phi) \cdot \nabla\eta & \text{on } \Gamma^f(t), \forall t \geq 0. \end{array} \right. \quad \begin{array}{l} (28a) \\ (28b) \\ (28c) \\ (28d) \\ (28e) \end{array}$$

As can be noticed taking a look at System (28), the use of the no slip formulation of the fully nonlinear free surface boundary condition presented in Equation 27 allows for a unified treatment of the bottom, body surface and free surface boundaries. Along with a simpler implementation, the extension of the boundary mesh displacement field \mathbf{v} to the basin bottom and hull boundaries, allows for the solution of a more general problem in which points on the latter boundaries are not necessarily idle, but are moving according to the prescribed velocity field \mathbf{v} . Only on the free surface boundary, the boundary points velocity field \mathbf{v} is unknown. Hence, to allow for its computation, in such region the additional Equation (20) is added.

3 Boundary value problem discretization

The literature on potential flow solvers with fully nonlinear free surface boundary conditions, suggests that the most common way to integrate over time and space a time dependent boundary value problem such as that in System (28), is the Mixed Eulerian-Lagrangian (MEL) scheme ([26]). In such a framework, at each time step a Laplace boundary value problem with Dirichlet boundary condition on the free surface is solved. After this, the kinematic boundary condition is time integrated to obtain the new position of the free surface, and the same is done with the dynamic boundary condition so as to obtain the new value of the free surface potential. With the new values of the free surface position and potential, a new time step can be processed. As is made clear by its name, the original MEL procedure was designed to work with the Lagrangian form of free surface boundary conditions. Yet a MEL-like algorithm can be also applied to semi-Lagrangian free surface conditions, as seen in [37]. Unfortunately, MEL cannot be applied to the free surface boundary condition formulation adopted in this work. In fact, the kinematic semi-Lagrangian free surface boundary condition has been here replaced with a non homogeneous Neumann boundary condition on such boundary, which makes MEL not applicable. Thus, we have resorted to

a different approach originally presented in [30], which consists in carrying out the spatial discretization of the governing problem, to obtain a system of Differential Algebraic Equations (DAE). In fact, the Boundary Element Method (BEM) discretization of the Laplace equation results in a set of algebraic equations, while the Finite Element Method (FEM) discretization of the free surface boundary conditions leads to a set of differential equations. The DAE combining these different equations is then solved by means of a Backward Difference Formula (BDF) time integration scheme. The next subsections will present details of the BEM and FEM used to discretize over space the Laplace equation and the dynamic free surface boundary condition, respectively. In addition, we will provide a description of the BDF time advancing scheme used to solve the resulting DAE system.

3.1 Laplace equation discretization based on Boundary Element Method

In this work, we make use of the Boundary Element Method (BEM) discretization method for the spatial discretization of the govern boundary value problem equations. In the context of fully nonlinear free surface potential flow simulation, this is quite a common choice. We must however remark that the Laplace equation for the velocity potential can be also discretized by means of the Finite Element Method (FEM). In this regard, noteworthy works have been carried out by Ma and Yan [27] and more recently by Bermudez et Al. [6]. At a first glance, it would appear that the most important advantage of BEM compared to FEM is the reduced number of unknowns associated with the codimension one grid. Unfortunately, in the practice such an advantage is typically offset by the presence of a dense resolution matrix in the discretized algebraic system. Yet, there are other advantages of BEM that made us favour it over FEM. In particular, in the context of the present physical problem, where moving boundaries such as the free surface are present, the codimension one grids required by BEM are much easier to generate, deform and manage without significant quality drop.

We use the same formalism presented in [14, 7, 12], the study a bounded open domain Ω with Lipschitz boundary $\Gamma = \partial\Omega$. To this end, System (28) is recast into the generic Laplace problem

$$-\Delta\phi = 0 \quad \text{in } \Omega \tag{29a}$$

$$\frac{\partial\phi}{\partial n} = f_N(\mathbf{x}) \quad \text{on } \Gamma_N \tag{29b}$$

$$\phi = f_D(\mathbf{x}) \quad \text{on } \Gamma_D, \tag{29c}$$

where Dirichlet and Neumann boundary conditions are imposed on the portions Γ_D , and Γ_N of $\partial\Omega$. We require that $\overline{\Gamma_D \cup \Gamma_N} = \partial\Omega$, $\Gamma_D \cap \Gamma_N = \emptyset$, we notice that $\Gamma_D \neq \emptyset$ ensures solution uniqueness.

3.1.1 Boundary integral formulation

We use the fundamental solution of the Laplace equation, called Green function [7], to rewrite (29a) as a Boundary Integral Equation (BIE)

$$\phi(\mathbf{x}) = \int_{\Gamma} G(\mathbf{x} - \mathbf{y}) \frac{\partial \phi}{\partial n}(\mathbf{x}) d\mathbf{s}_y - \int_{\Gamma} \phi(\mathbf{x}) \frac{\partial G}{\partial n}(\mathbf{x} - \mathbf{y}) d\mathbf{s}_y \quad \forall \mathbf{x} \in \Omega. \quad (30)$$

From (30) we notice that if the solution and its normal derivative on the boundary Γ are known then the potential ϕ can be computed in any point of the domain. Considering the trace of (30) we can write the boundary integral form of the original problem as

$$\alpha(\mathbf{x})\phi(\mathbf{x}) = \int_{\Gamma} G(\mathbf{x} - \mathbf{y}) \frac{\partial \phi}{\partial n}(\mathbf{x}) d\mathbf{s}_y - \int_{\Gamma}^{PV} \phi(\mathbf{x}) \frac{\partial G}{\partial n}(\mathbf{x} - \mathbf{y}) d\mathbf{s}_y \quad \text{on } \Gamma \quad (31a)$$

$$\frac{\partial \phi}{\partial n} = f_N(\mathbf{x}) \quad \text{on } \Gamma_N \quad (31b)$$

$$\phi = f_D(\mathbf{x}) \quad \text{on } \Gamma_D, \quad (31c)$$

where we have considered the Cauchy Principal Value (CPV) of the second integral. Then we write explicitly the boundary conditions (29a) in (31) obtaining

$$\begin{aligned} & \chi_{\Gamma_N}(\mathbf{x})\alpha(\mathbf{x})\phi(\mathbf{x}) - \int_{\Gamma_D} G(\mathbf{x} - \mathbf{y}) \frac{\partial \phi}{\partial n}(\mathbf{x}) d\mathbf{s}_y + \int_{\Gamma_N}^{PV} \phi(\mathbf{x}) \frac{\partial G}{\partial n}(\mathbf{x} - \mathbf{y}) d\mathbf{s}_y \\ &= -\chi_{\Gamma_D}(\mathbf{x})\alpha(\mathbf{x})f_D(\mathbf{x}) + \int_{\Gamma_N} G(\mathbf{x} - \mathbf{y})f_N(\mathbf{x}) d\mathbf{s}_y - \int_{\Gamma_D}^{PV} f_D(\mathbf{x}) \frac{\partial G}{\partial n}(\mathbf{x} - \mathbf{y}) d\mathbf{s}_y. \end{aligned} \quad (32)$$

We remark that $\alpha(\mathbf{x})$ is obtained from the CPV evaluation of the integral involving the derivative of the Green function, usually it represents the fraction of solid angle of the domain Ω seen from the boundary point \mathbf{x} . We use the generic characteristic function χ_A (which is one if $\mathbf{x} \in A$) to split the term $\alpha(\mathbf{x})\mathbf{x}$ between Neumann and Dirichlet boundaries.

3.1.2 Discretisation

The numerical discretization of (32) leads to a real Boundary Element Method (BEM). The resolution of a BEM requires the discretization of the unknowns using functional spaces defined on a Lipschitz boundary. We address this problem introducing suitable discretizations for the unknowns ϕ and $\frac{\partial \phi}{\partial n}$ based on standard Lagrangian finite element spaces on Γ . We use the same functional space to describe the geometry, this setting is often referred to as Isoparametric BEM.

We define the computational mesh as a quadrilateral decomposition Γ_h of the boundary Γ . We require that two cells K, K' of the mesh only intersects

on common edges or vertices, and that there exist a mapping from a reference cell \hat{K} to K whose Jacobian is uniformly bounded away from zero for all cells K . To ease the mesh generation time we allow the user to define a coarse grid and that we provide the tools to refine it on a required geometry. Following [13, 3] we provide some native shapes (as spheres, toruses, cubes, pyramids, *etc.*) and we offer an interface to CAD files which are the most common tool to define arbitrary geometrical descriptions [16, 4, 2]. This features has been employed in ship-wave simulations through BEM, [30, 28, 31], and [12] presents an example of an aeronautics-like NACA wing shape.

If ϕ and $\frac{\partial\phi}{\partial n}$ must lie in the spaces V and Q , defined as

$$V := \left\{ \phi \in H^{\frac{1}{2}}(\Gamma) \right\}$$

$$Q := \left\{ \gamma \in H^{-\frac{1}{2}}(\Gamma) \right\},$$

where $\Gamma = \partial\Omega$, then the integrals in equation (31a) are bounded. $H^{\frac{1}{2}}(\Gamma)$ is the space of traces on Γ of functions in $H^1(\Omega)$, while $H^{-\frac{1}{2}}(\Gamma)$ is its dual space. We construct the discretized spaces V_h and Q_h as conforming finite dimensional subspaces of V and Q respectively,

$$V_h := \left\{ \phi_h \in L^2(\Gamma_h) : \phi_h|_K \in \mathbb{Q}^r(K), K \in \Gamma_h \right\} \equiv \text{span}\{\psi_i\}_{i=1}^{N_V} \quad (33a)$$

$$Q_h := \left\{ \gamma_h \in L^2(\Gamma_h) : \gamma_h|_K \in \mathbb{Q}^s(K), K \in \Gamma_h \right\} \equiv \text{span}\{\omega_i\}_{i=1}^{N_Q}, \quad (33b)$$

where on each cell K $\phi_h|_K, \gamma_h|_K$ are polynomial functions of degree r and s respectively, in each coordinate direction. Following [12] we use iso-parametric discretisations based on standard Q_N Lagrangian finite elements, and by collocating the support points of the geometry patches directly on the CAD surfaces. We use the double nodes technique, [15], to ensure accuracy in the resolution of the BEM even when sharp edges are present.

The collocation method is a common resolution technique for a BEM since it does not require any additional integration of (32). For a deeper analysis of the accuracy of this setting the reader is referred to [12]. Collocating (31a) produces the linear system

$$(\alpha + N)\hat{\phi} - D\hat{\gamma} = 0, \quad (34)$$

where

- α is a diagonal matrix with the values $\alpha(x_i)$, where x_i represents the i -th collocation point;
- $N_{ij} = \sum_{k=1}^K \sum_{q=1}^{N_q} \frac{\partial G}{\partial n}(x_i - x_q) \psi_q^j J^k$, where \hat{K} represents the reference cell and J^k is the determinant of the first fundamental form for each panel k ;

- $D_{ij} = \sum_{k=1}^K \sum_q^{N_q} G(x_i - x_q) \psi_q^j J^k$;
- $\hat{\phi}, \hat{\gamma}$ represent the nodal value of potential and potential normal derivative.

When the collocation point lie inside the cell where we are integrating we use bidimensional Telles, Lachat Watson or Duffy quadrature formula, [39, 32] quadrature schemes, otherwise we use standard Gauss integration rules.

3.1.3 Numerical Implementation

We use [13] as a backbone library for our work. In particular we use High Performance Computing libraries as `deal.II` [3] and Trilinos [17] to split the computational load between different processors and to tackle linear algebra. We achieve multicore parallelism using Intel Threading Building Block (TBB) [35]. A similar combination has been successfully applied to achieve high computational efficiency in fluid dynamics, as demonstrated in ASPECT [25]. We remark that our BEM implementation greatly benefits from the distributed memory parallelism, due to the structure of the matrix assembling procedures.

3.2 Dynamic free surface boundary condition spatial discretization

Following the procedure outlined in [30], to tackle the numerical discretization of Equation (20), we resort to its weak form, which reads

$$\begin{aligned} \left(\frac{\delta \phi}{\delta t}, \mathbf{w} \right) &= \left(\frac{1}{2} |\mathbf{U}_\infty + \nabla \phi|^2 + \frac{1}{2} |\mathbf{U}_\infty|^2 - \mathbf{g} \cdot \mathbf{x} + (\mathbf{v} - \mathbf{U}_\infty - \nabla \phi) \cdot \nabla \eta, \mathbf{w} \right) \\ &= (b^\phi, \mathbf{w}). \end{aligned} \quad (35)$$

Here, $\mathbf{w} \in V$ is a test function and the notation

$$\begin{aligned} (a, b)_w &= \int_{\Gamma^w(t)} ab \, d\Gamma \\ (a, b) &= \int_{\Gamma(t)} ab \, d\Gamma \end{aligned} \quad (36)$$

indicates a scalar product in the space $L^2(\Gamma)$. The discretization of Equation (35) is carried out by means of a Galerkin Finite Element Method (FEM) based on the shape functions defined in Equation (33), and results in the following system of algebraic equations

$$M\widehat{\dot{\phi}} = \mathbf{b}^\phi \quad (37)$$

where

- M is a sparse mass matrix, the entries of which are given by $M_{ij} = (\psi_j, \psi_i)$;
- \mathbf{b}^ϕ is a right hand side vector, with entries given by $\mathbf{b}_i^\phi = (b^\phi, \psi_i)$;
- the entries of vector $\widehat{\dot{\phi}}$ represent the nodal values of potential ALE time derivative $\frac{\delta\phi}{\delta t}$.

There are several advantages associated with such an L^2 projection approach. First, it avoids the evaluation of the potential gradients and surface normal vectors in correspondence with the free surface collocation points, where such quantities are not single valued. In fact, the integrals appearing in the weak formulation only require the right hand side of Equation (20) to be evaluated on the numerical integration scheme quadrature nodes, which fall within each quadrilateral cell. At such location, the potential gradients and surface normal vectors are single valued, which results in an accurate spatial integration scheme. An additional advantage is that matrix M is sparse, so assembling it only leads to a modest computational overhead with respect to only assembling the BEM matrix. Finally, a further advantage of the L^2 projection approach, is that Equation (37) can be readily modified to include stabilization terms able to avoid the dominant transport instabilities occurring for high stream velocity, and discussed in Section 2.2.2. As in [30], we make use of a Streamwise Upwind Petrov–Galerkin (SUPG) stabilization (for more detail, see [19, 40]) strategy to suppress free surface instabilities that initially lead to in saw-tooth shaped free surface and eventually result in simulation blow up. The SUPG stabilization consists in replacing the plain L^2 projection in System (37) with the weighted projection

$$\widetilde{M}\widehat{\dot{\phi}} = \widetilde{\mathbf{b}}^\phi \quad (38)$$

where

- The entries of \widetilde{M} are given by $\widetilde{M}_{ij} = (\psi_j, \psi_i + \mathbf{d} \cdot \nabla_s \psi_i)$;
- The entries of the right hand side vector $\widetilde{\mathbf{b}}^\phi$ are given by $\widetilde{\mathbf{b}}_i^\phi = (b^\phi, \psi_i + \mathbf{d} \cdot \nabla_s \psi_i)$;
- Vector $\mathbf{d} = \tau \frac{\mathbf{v} - \mathbf{U}_\infty - \nabla \phi}{\|\mathbf{v} - \mathbf{U}_\infty - \nabla \phi\|}$ is aligned with the local velocity direction, with τ being a scalar coefficient proportional to the local mesh size.

3.3 Time advancing scheme

The spatially discretized resolution system can be recast in the following form

$$F(\dot{\mathbf{y}}, \mathbf{y}, t) = 0 \quad (39)$$

where

$$\mathbf{y}(t) = \begin{Bmatrix} \{\mathbf{x}\} \\ \{\hat{\phi}\} \\ \{\hat{\gamma}\} \end{Bmatrix} \quad (40)$$

and $\{\mathbf{x}\}$ is the vector containing the coordinates of all the collocation points (or degrees of freedom) of the BEM problem. As will be discussed in more detail in Section 4.1, to test the effectiveness of the free surface boundary condition formulation proposed and avoid other sources of error, in this work we only consider the case of a fully submerged body advancing in calm water. For such a reason the equations in System (39) that refer to the horizontal coordinates of all the collocation points, will translate the fact that no horizontal motion is prescribed. As for the vertical coordinates, the displacements — and velocities — will be set to 0 for all the collocation points, except for the ones on the free surface. In correspondence with such nodes, the system equations will be obtained from System 38, which represents the discretized and stabilized version of the ALE free surface dynamic boundary condition. Note that the grid velocity field \mathbf{v} appearing in the ALE free surface and non homogeneous Neumann boundary conditions, is simply the time derivative $\{\dot{\mathbf{x}}\}$ of the collocation point coordinates. Finally, as for the the system degrees of freedom associated with the potential $\hat{\phi}$ and potential normal derivative $\hat{\gamma}$ collocation point values, the BEM resolution Equations (34) are used.

Equation (39) represents a system of nonlinear differential algebraic equations (DAE), which we solve using the IDA package of the SUNDIALS OpenSource library [18]. A $1e-5$ relative residual tolerance is set for the Newton iterations used to solve the nonlinear problem arising at each time step from the implicit time discretization scheme.

3.4 DAE restart procedure

A noteworthy feature of the solver developed, is that the time integration is periodically paused to allow for adaptive grid refinement. At each refinement cycle, a Kelly error estimator ([22, 11, 1]) is computed based on the water elevation field η . After the cells are sorted according to the error indicator, a prescribed fraction of them having the highest values are flagged and eventually refined.

Once the grid refinement has been carried out, all the fluid dynamic fields are interpolated onto the new mesh. Of course, the interpolated solutions

will not satisfy the DAE residual in Equation (39). Since a non null initial residual normally leads to simulation blowup, the solution must be adjusted at each restart, so as to satisfy Equation (39). In the model discussed in [30], at each start, the solution $\bar{\mathbf{y}}$ was obtained through interpolation of the coarse grid solution on the new grid. Then the restart solution time derivative $\dot{\mathbf{y}}^r$ was computed as the solution of the following nonlinear equation system

$$F(\dot{\mathbf{y}}^r, \bar{\mathbf{y}}, t^r) = G(\dot{\mathbf{y}}^r) = 0. \quad (41)$$

System (41) is solved by means of a Newton–Raphson algorithm implemented in the KINSOL package of the SUNDIALS OpenSource library [18]. Also in this case, a $1e-5$ relative residual tolerance is set for the Newton iterations. The approach just described, which consists in imposing the interpolated nodes positions to obtain the nodes velocities satisfying the DAE residual, did not lead to optimal results. In fact, it resulted in very high nodes velocities which had to compensate for the slightly incorrect positioning of the nodes due to interpolation error. As a result, the time steps at each restart had to drop to follow the faster dynamics, slowing down the simulation.

A much more interesting alternative restart treatment, is that of imposing the interpolated solution time derivative $\bar{\dot{\mathbf{y}}}$, to obtain the solution from the DAE residual, namely

$$F(\bar{\mathbf{y}}, \mathbf{y}^r, t^r) = G(\mathbf{y}^r) = 0. \quad (42)$$

This approach does not introduce spurious fast dynamic components, and is of course to be preferred. Unfortunately, numerical evidence suggests that if used — as is the case for [30] — in presence of the semi-Lagrangian kinematic and dynamic boundary conditions (19) and (20), Problem (42) is not well posed, likely due to a singular Jacobian $\frac{\partial F}{\partial \mathbf{y}}$. On the other hand, the introduction of the alternative formulation adopted in the present work, allows for the solution of Problem (42), obtaining correct restart solution without introducing spurious faster dynamics into the DAE system. In addition, as will be explained in next session, the correct solution of Problem (42) has been the gateway to the possibility of solving steady problems.

3.5 Stationary solver

As discussed at length, both the mathematical formulation of the free surface boundary condition, and the numerical discretization of the resulting boundary value problem have been selected so that stationary and non stationary problems could have a unified implementation. To write the problem for the stationary solution \mathbf{y}^s , we introduce the additional conditions $t \rightarrow \infty$ and $\dot{\mathbf{y}} = 0$ in System (39), namely

$$F(\dot{\mathbf{y}}^0, \mathbf{y}^s, t \rightarrow \infty) = G(\mathbf{y}^s) = 0. \quad (43)$$

To obtain a unified implementation for steady and unsteady solvers, the nonlinear System (43) is solved making use of the same residual function implemented for the DAE solver, in which the $\dot{\mathbf{y}}$ argument is set to zero at every call. The resulting problem is by all means a particular case of Problem (42), and such a nonlinear system of equations for \mathbf{y}^s is again solved by means of a Newton–Raphson algorithm implemented in the KINSOL package of the SUNDIALS OpenSource library. As will be shown, this resulted in a software in which it is possible to switch from non stationary to stationary solver at the sole cost of including or not including time derivatives upon numerical resolution of the DAE system. This is of course more straightforward than using a set of completely different non linear free surface boundary conditions for unsteady and steady potential flow problems.

4 Results

A simulation campaign has been carried out to fully characterize the performance of the algorithm proposed. In particular, to reproduce the possible practical use of a potential flow solver suited for early design stages, all the numerical tests have been carried out on an Intel Quad Core i7-7700HQ 2.80GHz, 16 GB RAM laptop. In addition, the academic test case considered allowed for cross validation through the comparison with well assessed literature results. The next sections will describe the details of the test case considered, and present the results of the simulation campaign.

4.1 The immersed ellipsoid test case description

The test case considered is that of a fully immersed ellipsoid advancing at steady speed in calm water. The prolate spheroid considered is moving in the direction of its horizontal axis of revolution and has a radius which is one fifth of its length. Figure 2 displays a two dimensional diagram reporting the dimensions of the computational domain employed throughout the simulation campaign, which is attached to the spheroid and is advancing in the water alongside with it. Most of the lengths reported in the picture are referred to the ellipsoid length $L = 10$ m. We also report that the overall width of the channel, which is not appreciable from this two dimensional sketch, was set to $10L$.

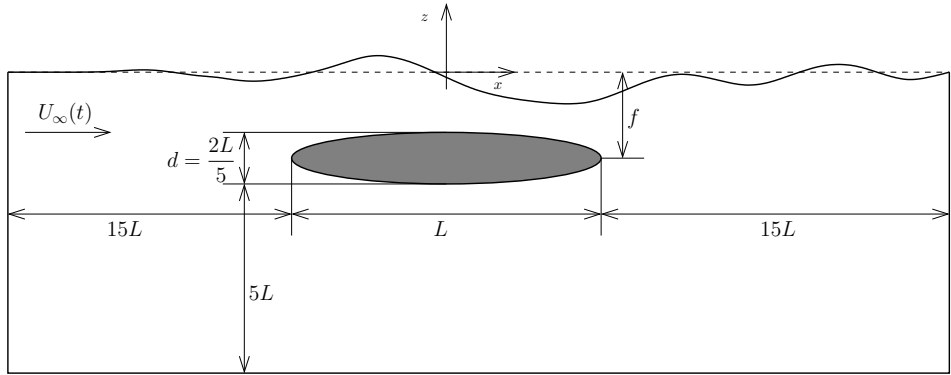


Figure 2: A two dimensional sketch illustrating the computational domain dimensions used for the fully immersed ellipsoid test case. All the lengths indicated in the diagram are referred to the ellipsoid length $L = 10$ m. In the simulation campaign, we have tested different values of the vertical distance f between the spheroid horizontal axis of revolution and the undisturbed free surface elevation, located at $z = 0$.

4.1.1 Steady state numerical experiments

A first set of experiments has been devoted to evaluate the performance of the steady flow solver developed, both in terms of computational cost and in terms of accuracy of the solutions. In this case, the asymptotic velocity magnitude $U_\infty(t) = \|\mathbf{U}_\infty(t)\|$ has been set to a constant value \bar{U}_∞ in each simulation considered. In such set of tests, several values of \bar{U}_∞ have been considered, as well as multiple values of the depth f — defined as the vertical distance between the spheroid horizontal axis of revolution and the undisturbed free surface elevation, located at $z = 0$. For a better evaluation of the results, the non dimensional version of the latter parameters will be reported in the next sections. The Froude number (namely $\text{Fr} = U_\infty(t)/(gL)$) will be used as the non dimensional measure of the asymptotic velocity, while the non dimensional ellipsoid distance from the undisturbed free surface will be indicated by the parameter d/f .

Making use of the CAD handling features of the π -BEM library [12], the very coarse quadrilateral mesh originally imported is automatically refined on the surface spheroid until it suitably represents the object geometry.

Figure 3 illustrates such process, which is made up of 7 adaptive refinement cycles based on the curvature. Throughout each refinement cycle, the CAD geometry is interrogated to compute the position of the new nodes on the spheroid surface, and to obtain evaluation of local curvature to flag cells

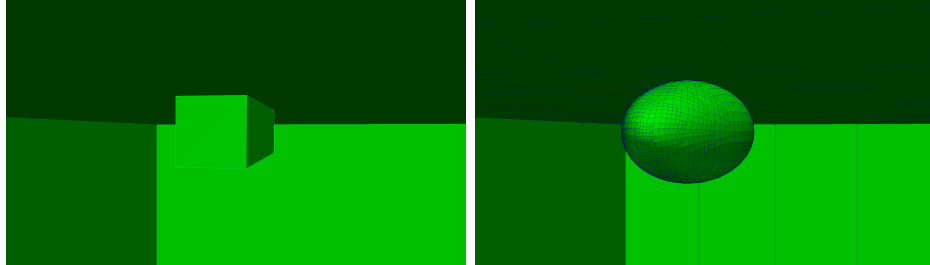


Figure 3: On the left, a view of the ellipsoid initial mesh, only composed of 4 cells. On the right, the same view of the ellipsoid mesh used for all the simulations. The latter mesh has been obtained through fully automated adaptive refinement cycles based on surface curvature, and interfaced with the ellipsoid CAD geometry.

for refinement. In such framework, the original coarse mesh (on the left in the figure) composed of 16 nodes is refined to obtain the simulation initial mesh featuring 2021 nodes (on the right in the figure). We also point out that the automated refinement process includes cycles to reduce the cells aspect ratios until they are lower than 3.5, and cycles to refine the region of the free surface closest to the ellipsoid.

The initial computational mesh described is depicted in Figure 4, on the left. The other plots in the Figure refer to further cycles of the adaptive refinement process based on surface elevation. In such process, once the initial mesh is available, the nonlinear problem resulting from the steady fluid dynamic equations is solved to compute the flow velocity potential and the water elevation. The latter field is then used to compute Kelly error estimator and flag for refinement the portion of free surface cells accounting for 50% of the total grid error estimate. The cycle is then repeated 8 additional times, to obtain the final grid depicted on the right of Figure 4. As expected, by a qualitative standpoint the computational grid refinement pattern appears to follow the V-shaped Kelvin wake induced by the spheroid underwater motion.

4.1.2 Unsteady numerical experiments

The unsteady flow simulations carried out in this work have been aimed at providing a numerical confirmation that the solver developed can indifferently operate under transient or steady flow assumptions. In particular, it is relevant showing that if a flow admits a regime solution that is constant over time, both the transient and the steady solver converge to the same result. Thus, to allow for such a comparison, we considered one of the steady test

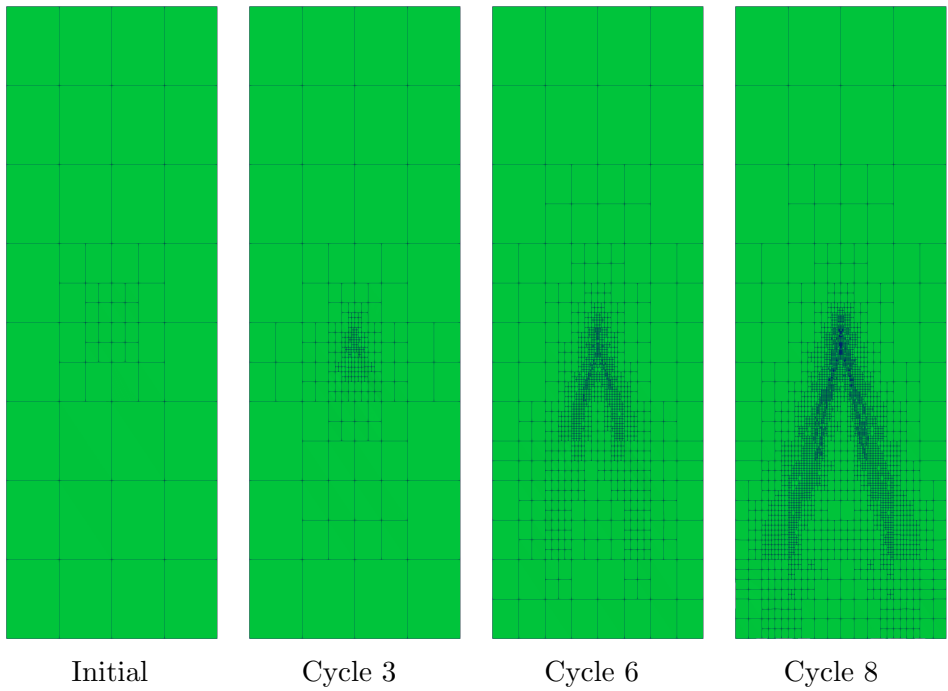


Figure 4: An illustration of the computational grids across the adaptive refinement process based on free surface elevation characterizing the simulations. From left to right, the top view of the free surface grid at Cycles 0, 3, 6, 8, respectively. As expected, the refinement pattern covers the Kelvin wave produced by the spheroid.

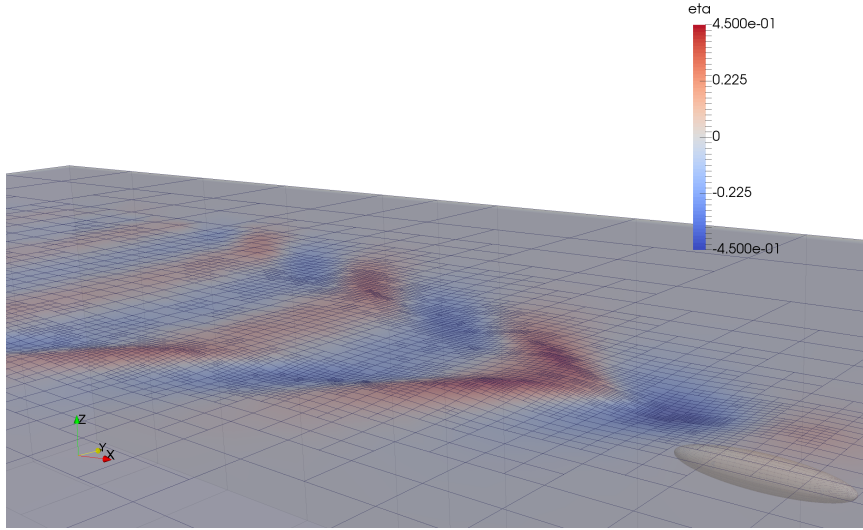


Figure 5: An illustration of the free surface elevation contour, and of the domain mesh. The plot refers to the $d/f = 0.8$ and $Fr = 0.6$ test case.

cases previously described, and solved with the transient solver. We focused in particular on the case in which the depth of the cylinder corresponded to $d/f = 0.8$ and $Fr = 0.8$. In the numerical experiments, we considered three different transient simulations in which the asymptotic velocity U_∞ is increased with sinusoidal ramps lasting 0.75 s , 7.5 s and 15 s , respectively. To obtain a fair comparison between steady and unsteady solver result, a steady simulation featuring 3 adaptive refinement cycles is first carried out. After this, the solution is reinitialized on the adaptively refined grid, and a transient simulation is started from rest, and run until a convergence to a regime solution is observed. This procedure allows for the evaluation of the wave resistance and lift forces obtained both with the steady and unsteady solver, when the same grid is used. Since, as explained in Section 3.5, the nonlinear problem residual used by both methods is the same, the two solutions are expected to be substantially identical.

4.2 Numerical results

A typical output of the simulations is portrayed in Figure 5. The picture refers to the $d/f = 0.8$ and $Fr = 0.6$ test case, and both the free surface and underwater spheroid mesh are visible. The free surface is colored according to contours of water elevation, which make visible the accurate reconstruction of the Kelvin wake pattern generated by the moving body.

We will now present the quantitative results of the campaign of numerical experiments described in Section 4.1. A first objective will be that of characterizing the performance of the adaptive refinement approach adopted in terms of both computational cost and convergence to a stable solution. After this, we will discuss the accuracy of the solutions obtained.

4.2.1 Steady case results

The overall computational cost of a typical simulation is reported in Table 1 — which more specifically refers to the stationary ellipsoid test case in which $Fr = 0.7$ and $d/f = 0.8$, solved on an Intel Quad Core i7-7700HQ 2.80GHz, 16 GB RAM laptop. For each line corresponding to a refinement cycle carried out, the columns of the Table report the number of computational grid nodes, along with the number of nonlinear iterations and Jacobians assemblies required by the Newton solver to reach convergence, and finally the execution time. As expected, the dimension of the grid grows at a faster rate in the latest refinement cycles. This is explained by the fact that only the portion of cells with highest error indicators which cumulatively represent a fixed fraction of the overall error is refined at every cycle. Thus, as more cycles are executed, such error gets distributed over a wider amount of cells, which will be then flagged for refinement. For the most part, the execution time of each cycle reported in the table mirrors the growth in the computational grid nodes — which are also the BEM problem degrees of freedom. The only factor perturbing the expected quadratic relationship between grid nodes and computational cost, is the number of nonlinear iterations and of Jacobians assemblies required by the Newton solver to converge at every cycle. The latter operation is in fact particularly time consuming, and can significantly affect the duration of a single simulation cycle. For instance, in the test case considered cycle 2 lasted significantly less than all the previous cycles characterized by smaller grids. This is exactly because the convergence of the Newton solver in such simulation only required that the Jacobian was assembled and factorized once, while it had to be assembled two times in the previous cycles. The overall computational cost of the entire refinement cycles procedure is approximately four hours, which is in principle compatible with simulations run in early hull design stages. In such framework, further refinement cycles might result in significantly higher computational cost and RAM memory occupation offering no significant accuracy gain. For such reason, they have not been considered in this work.

Figure 6 allows for an evaluation of the adaptive refinement cycles effectiveness in converging to a stable solution. The left diagram in the Figure

Refinement cycle	Grid nodes	Nonlinear iteratios	Jacobians assembled	Execution time
0	2021	4	2	0 h 05 m 22 s
1	2073	5	2	0 h 05 m 46 s
2	2139	6	2	0 h 06 m 16 s
3	2284	5	1	0 h 03 m 56 s
4	2510	6	1	0 h 05 m 01 s
5	3000	6	1	0 h 07 m 36 s
6	3798	7	1	0 h 13 m 47 s
7	5275	5	1	0 h 29 m 50 s
8	7775	12	2	2 h 52 m 00 s

Table 1: Grid nodes, number of Jacobian matrices assembled and overall computational times required for each adaptive refinement cycles. The values reported refer to the stationary ellipsoid test case in which $\text{Fr} = 0.7$ and $d/f = 0.8$, solved on an Intel Quad Core i7-7700HQ 2.80GHz, 16 GB RAM laptop.

shows the typical evolution of the steady state hydrodynamic lift across 8 adaptive refinement cycles. The plot refers to the stationary test case in which $\text{Fr} = 0.7$ and $d/f = 0.8$. As can be appreciated, the hull hydrodynamic lift gradually decreases to values lower than the hydrostatic lift ($L_0 = 209010.89$ N), and appears to settle in the last two iterations to values that are approximately 1.3% shorter than L_0 .

The grid convergence trend is further confirmed by the left plot in Figure 6, which depicts the wave resistance evolution across 8 refinement cycles. The plot refers again to the stationary test case in which $\text{Fr} = 0.7$ and $d/f = 0.8$. Starting from low values obtained with the initial coarse grids, the resistance values gradually increase across refinements, until the last refinement cycle considered result in no significant resistance variation.

The results presented in Figure 6 suggest that for the ellipsoid test case under study grid convergence is obtained at the 7th refinement cycle. In fact, the wave resistance and lift forces computed at the 7th refinement cycle only differ by 0.3% and 0.7%, respectively, from the values computed at the 8th and final refinement. Based on the computational costs reported in Table 1, it can be inferred that a reliable drag and lift prediction is obtained in approximately 1 h 15 m on a laptop. Figure 7 provides a confirmation that such trend holds across all the range of Froude numbers investigated. The plots in the Figure show the values on non dimensional net lift $L^* =$

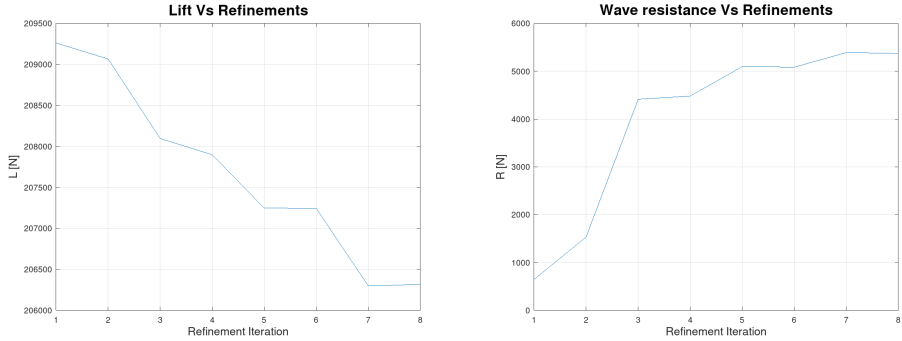


Figure 6: Fully immersed ellipsoid dimensional lift (left) and resistance (right) value as a function of adaptive refinement iterations. The curve refers to the stationary ellipsoid test case in which $\text{Fr} = 0.7$ and $d/f = 0.8$.

$(L - L_0)/L_0$ (left) and non dimensional wave resistance $R^* = (R)/L_0$ (right) as a function of Fr . In both diagrams the diamonds indicate the results obtained at the 7th adaptive refinement cycle, while the asterisks refer to the results obtained at the 8th cycle. For reference, continuous lines representing corresponding literature results by Scullen [38] have been added to the plot. As can be appreciated in all the test cases considered the difference between the solution at the last two refinement cycles is minimal, even compared to the difference observed with different models solutions.

To provide the reader with an extensive assessment the accuracy of the model proposed, we compare the nondimensional forces computed with the present method against similar results reported in [38]. In such work, Scullen made use of a steady potential flow solver with fully nonlinear free surface boundary conditions which represent a combination of the null pressure and null pressure total derivative requirement. Figure 8 compares the non dimensional net lift values obtained in this work (indicated by asterisks) against the corresponding results obtained by Scullen (solid lines). The different curves in the plot represent non dimensional net lift as a function of Fr obtained imposing different values of the $\frac{d}{f}$ ratio. The results show good agreement with Scullen data throughout the Fr and $\frac{d}{f}$ ranges tested. The plot also indicates that the most appreciable differences are observed for higher Fr and $\frac{d}{f}$ values, where the present method lift is consistently higher than its reference counterpart. This might be a result of the different — and possibly less dissipative — BEM formulation in which Rankine sources coincide with collocation nodes, and special singular quadrature is used. Such formulation might result in higher free surface nodes displacements which

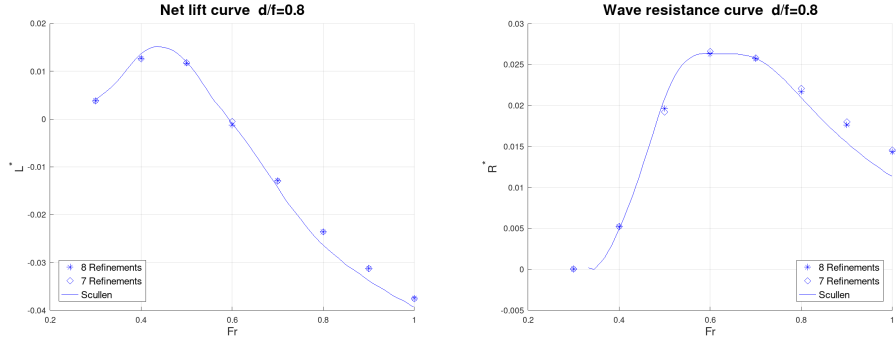


Figure 7: Fully immersed ellipsoid non dimensional net lift $L^* = (L - L_0)/L_0$ (left) and resistance $R^* = (R)/L_0$ (right) as a function of Froude number Fr . For reference, the continuous lines refers to results obtained by Scullen for ellipsoid depth to diameter ratio $d/f = 0.8$. The results obtained at the 7th and 8th adaptive refinement iterations are indicated by diamonds and asterisks, respectively.

bring the free surface closer to the spheroid in the stern region, leading to increased local speeds associated with upwards suction.

Figure 9 displays a comparison of non dimensional wave resistance values obtained in this work (indicated by asterisks) against the corresponding results obtained by Scullen (solid lines). The different curves in the plot represent non dimensional resistance as a function of Fr obtained imposing different values of the $\frac{d}{f}$ ratio. Also in this case, the results seem in good agreement with their reference literature counterparts across all the range of Fr and $\frac{d}{f}$ values considered. Once again, the most relevant differences are observed in correspondence with the highest Fr and $\frac{d}{f}$ tested, where the wave drag predicted by the present method is consistently and sensibly higher than the value reported by Scullen. This can once again be ascribed to the less dissipative nature of the solver proposed, which predicts higher surface displacements bringing the free surface closer to the hull in the stern region. This generates higher suction and, in turn, an additional drag due to lower pressures in the stern region.

We must finally remark that as Figures 8 and 9 suggest, some solutions have been obtained with the present method in regions where previous methods seem not reach convergence. This is particularly evident for $\frac{d}{f} = 1$ and

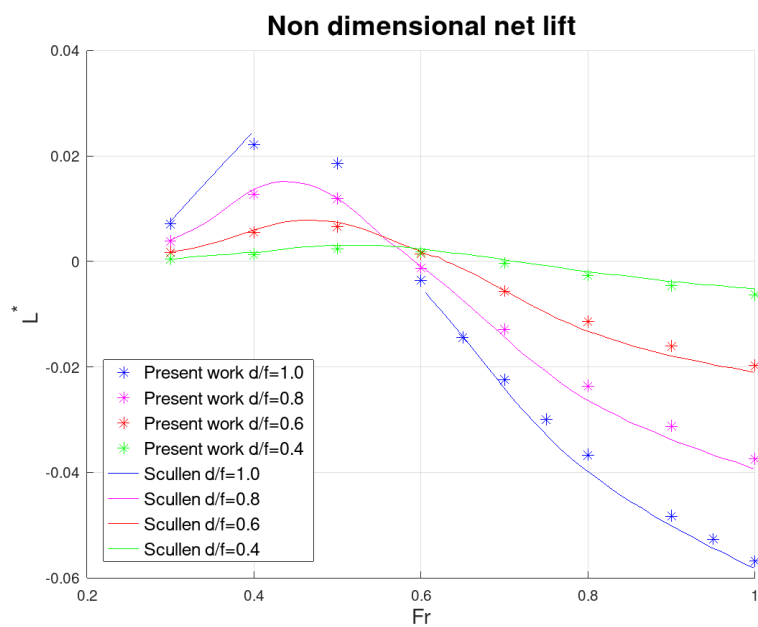


Figure 8: Fully immersed ellipsoid non dimensional net lift $L^* = (L - L_0)/L_0$ as a function of Froude number Fr . The differently colored continuous lines refer to results obtained by Scullen for values of ellipsoid depth to diameter ratio $d/f = 1.0, 0.8, 0.6, 0.4$. The results obtained in this work are indicated by asterisks with corresponding colors.

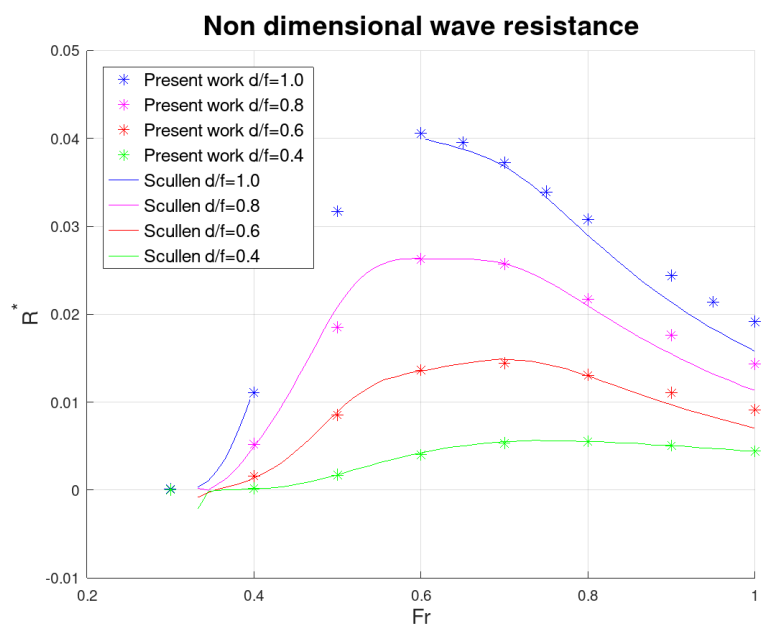


Figure 9: Fully immersed ellipsoid non dimensional wave resistance $R^* = (R)/L_0$ as a function of Froude number Fr . The differently colored continuous lines refer to results obtained by Scullen for values of ellipsoid depth to diameter ratio $d/f = 1.0, 0.8, 0.6, 0.4$. The results obtained in this work are indicated by asterisks with corresponding colors.

$\text{Fr} = [0.4, 0.6]$, for which no solution is reported by Scullen. This should not surprise, as in such conditions the deepest wave trough is located slightly above the ellipsoid stern region, and almost contact is reached between the free surface and the hull. In the framework of the current method implementation, no contact between free surface and disturbing body is considered. Moreover, the non desingularized method used has currently no mechanism in place to apply singular quadrature on the hull stern surface and account for the very close Rankine sources in the free surface trough, and vice versa. For such reason, also in this work some simulations failed to reach convergence at the 8th refinement level. Thus, we must report that the ability to predict hydrodynamic forces in such condition is a result of the adaptive refinement approach adopted rather than a product of a superior robustness. Yet, being able to obtain a solution with a locally less refined grid, gives us the opportunity to obtain a viable drag and lift estimate also in such difficult test case.

4.2.2 Unsteady case results

The numerical results of the unsteady test cases described in Section 4.1.2 are now taken into consideration. Figure 10 presents a plot of the underwater ellipsoid wave resistance force absolute value as a function of time. The blue, green and magenta continuous lines refer to the test cases in which the flow asymptotic velocity \mathbf{U}_∞ reaches the target value after sinusoidal ramps of 0.75 s, 7.5 s and 15 s, respectively. The diagram clearly shows that all the test cases considered gradually reach the same constant regime solution. For the purposes of the present work, it is important to point out that the wave resistance value associated with such a common regime solution is identical to the one obtained with the steady state simulation on the same computational grid, denoted by the dashed red line in the plot. On one hand, this should not be a surprise, as the nonlinear problems solved for the steady and unsteady solver are substantially the same if $t \rightarrow \infty$, as illustrated in Section 3.5. On the other hand, it must be stressed that obtaining a potential flow solver with fully nonlinear free surface treatment and the ability to compute both transient and steady solutions, is one of the main objectives of this work. A further look at the time evolution plot for the three test cases, shows that, as expected, the test case with faster dynamics (blue line) results in a higher peak resistance associated with the added mass contribution induced by the increased initial acceleration. As a consequence of this, also the rebound resistance local minimum following the initial water acceleration past the hull, is more intense in the 0.75 s test case.

Unsteady vs Steady solver wave resistance

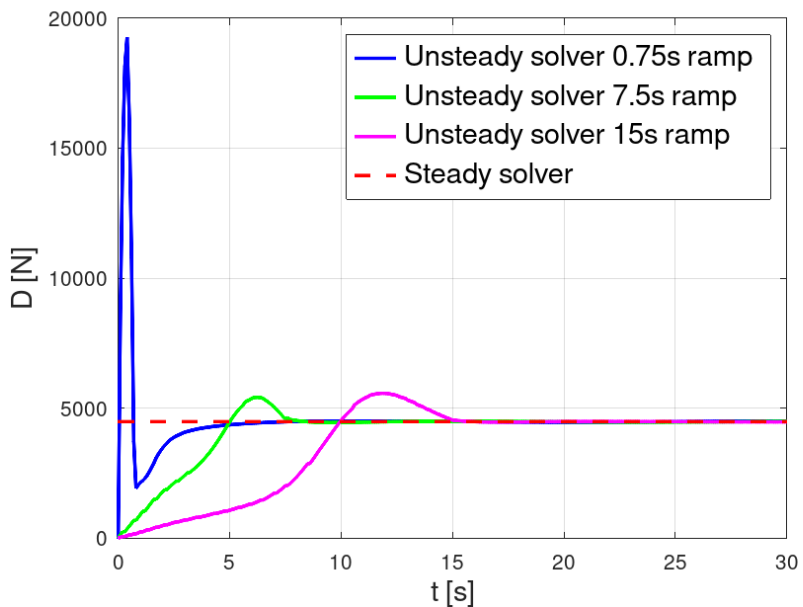


Figure 10: Wave resistance as a function of time for the fully immersed ellipsoid with $d/f = 0.8$ advancing at a regime speed corresponding to $Fr = 0.8$. The red dashed curve represents the result obtained with the steady solver after 3 adaptive refinement cycles. The unsteady solver simulation results obtained with a 0.75 s , 7.5 s and 15 s are displayed by the blue, green and magenta curve, respectively.

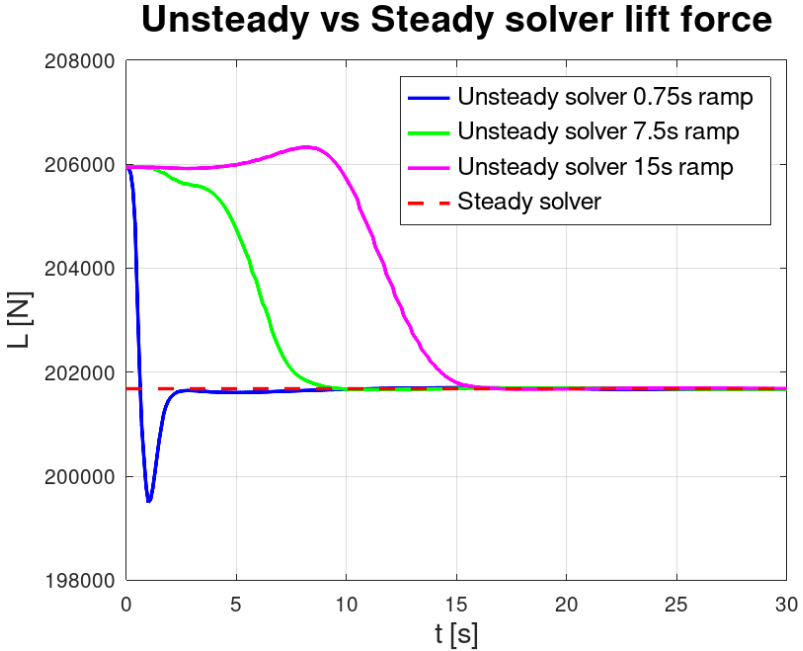


Figure 11: Hydrodynamic lift as a function of time for the fully immersed ellipsoid with $d/f = 0.8$ advancing at a regime speed corresponding to $Fr = 0.8$. The red dashed curve represents the result obtained with the steady solver after 3 adaptive refinement cycles. The unsteady solver simulation results obtained with a 0.75 s, 7.5 s and 15 s are displayed by the blue, green and magenta curve, respectively.

Figure 11 depicts absolute values of hydrodynamic lift acting on the immersed ellipsoid, as a function of time. In the diagram, the lines color are associated to the 0.75 s, 7.5 s and 15 s ramp test cases, in the same way reported for the wave resistance plot. The lift plots substantially confirm what previously observed analyzing the resistance results. Also in this case, all the unsteady flow solver results appear to converge to a common steady state lift value, which coincides with the value resulting from the steady solver simulation on the same grid.

5 Conclusions and future perspectives

This work presented a novel formulation of the fully nonlinear free surface boundary conditions which complement the Laplace equation in numerical towing tank based on unsteady potential flow theory. The main advantage of the unsteady free surface model discussed, is that it can lead to steady

state solutions once the — null — time derivatives are eliminated by the discretized problem. Such a feature, as discussed, is not common in fully nonlinear potential flow solvers available in the literature and in the commercial software market. Numerical results presented confirm that the steady and unsteady solvers result in the same solution for long time integration, and that the steady solver solutions are in close comparison with classical steady nonlinear free surface potential solvers.

A possible immediate future work perspective, is including a time dependent Dirichlet or Neumann inflow boundary condition to introduce a set of desired waves in the domain, and evaluate wave induced added resistance. In addition, the CAD interface ([28]) and Fluid Structure interaction solver for rigid ships ([29]) should be implemented also in the present software to obtain a versatile and effective numerical towing tank. Also adding the effect of lifting surfaces as in [36] would result in including the effects of hull appendages in the model.

Finally, we must point out that the free surface boundary condition in ALE form used in this work do not depend on the assumption that the free surface η is a single valued Cartesian function. In fact, it is only through Equation (21) that such constraint is introduced in the system, whereas Equations (27) and (20) are the ALE version of the non penetration and dynamic free surface condition, and can in principle work with any grid velocity field \mathbf{v} . Thus, future work will investigate the possibility of reproducing steep or overturning waves in the present formulation, through a wiser \mathbf{v} choice.

6 Acknowledgments

We acknowledge the support by the European Commission H2020 ARIA (Accurate ROMs for Industrial Applications, GA 872442) project, by MIUR (Italian Ministry for Education University and Research) and PRIN "Numerical Analysis for Full and Reduced Order Methods for Partial Differential Equations" (NA-FROMPDEs) project, and by the European Research Council Consolidator Grant Advanced Reduced Order Methods with Applications in Computational Fluid Dynamics-GA 681447, H2020-ERC COG 30 2015 AROMA-CFD.

References

- [1] M. Ainsworth and J.T. Oden. A posteriori error estimation in finite element analysis. *Computer Methods in Applied Mechanics and Engineering*, 142(1-2):1–88, 1997.

- [2] D. Arndt, W. Bangerth, D. Davydov, T. Heister, L. Heltai, M. Kronbichler, M. Maier, J.-P. Pelteret, B. Turcksin, and D. Wells. The **deal.II** library, version 8.5. *Journal of Numerical Mathematics*, 2017.
- [3] Daniel Arndt, Wolfgang Bangerth Marco Feder, Marc Fehling, Rene Gassmöller, Timo Heister, Luca Heltai, Martin Kronbichler, Matthias Maier, Peter Munch, Jean-Paul Pelteret, Simon Sticko, Bruno Turcksin, and David Wells. The **deal.II** library, version 9.4. *Journal of Numerical Mathematics*, 2022. Accepted.
- [4] Wolfgang Bangerth, Denis Davydov, Timo Heister, Luca Heltai, Guido Kanschat, Martin Kronbichler, Matthias Maier, Bruno Turcksin, and David Wells. The **deal.II** library, Version 8.4. *Journal of Numerical Mathematics*, 24(3):135–141, 2016.
- [5] R. F. Beck. Time-domain computations for floating bodies. *Applied Ocean Research*, 16:267–282, 1994.
- [6] A. Bermúdez, O. Crego, and A. Prieto. Upwind finite element-pml approximation of a novel linear potential model for free surface flows produced by a floating rigid body. *Applied Mathematical Modelling*, 103:824–853, 2022.
- [7] C A Brebbia. *The Boundary Element Method for Engineers*. Pentech Press, 1978.
- [8] Y. Cao, R. F. Beck, and W. Schultz. An absorbing beach for numerical simulations of nonlinear waves in a wave tank. *Proceedings of the 8th international workshop on water waves and floating bodies, St. John's, Newfoundland*, 1993.
- [9] Jean Donea, Antonio Huerta, J.-Ph. Ponthot, and A. Rodríguez-Ferran. *Arbitrary Lagrangian–Eulerian Methods*, chapter 14. John Wiley & Sons, Ltd, 2004.
- [10] Luca Formaggia, Alfio Quarteroni, and Alessandro Veneziani. Cardiovascular mathematics : modeling and simulation of the circulatory system. 2009.
- [11] D.S.R. Gago, DW Kelly, OC Zienkiewicz, and I. Babuska. A posteriori error analysis and adaptive processes in the finite element method: Part II–Adaptive mesh refinement. *International journal for numerical methods in engineering*, 19(11):1621–1656, 1983.
- [12] Nicola Giuliani, Andrea Mola, and Luca Heltai. π -bem: A flexible parallel implementation for adaptive, geometry aware, and high order boundary element methods. *Advances in Engineering Software*, 121:39 – 58, 2018.

- [13] Nicola Giuliani, Andrea Mola, and Luca Heltai. pi-BEM: Parallel BEM Solver. <https://github.com/mathLab/pi-BEM>, 2021.
- [14] Nicola Giuliani, Andrea Mola, Luca Heltai, and Luca Formaggia. FEM SUPG stabilisation of mixed isoparametric BEMs : Application to linearised free surface flows. *Engineering Analysis with Boundary Elements*, 59:8–22, oct 2015.
- [15] S. T. Grilli, P. Guyenne, and F. Dias. A fully non-linear model for three-dimensional overturning waves over an arbitrary bottom. *Journal for Numerical Methods in Fluids*, 35(7):29–67, 2015.
- [16] Luca Heltai, Wolfgang Bangerth, Martin Kronbichler, and Andrea Mola. Propagating geometry information to finite element computations. *ACM Trans. Math. Softw.*, 47(4), sep 2021.
- [17] Michael a. Heroux, Eric T. Phipps, Andrew G. Salinger, Heidi K. Thornquist, Ray S. Tuminaro, James M. Willenbring, Alan Williams, Kendall S. Stanley, Roscoe a. Bartlett, Vicki E. Howle, Robert J. Hoekstra, Jonathan J. Hu, Tamara G. Kolda, Richard B. Lehoucq, Kevin R. Long, and Roger P. Pawlowski. An overview of the Trilinos project. *ACM Transactions on Mathematical Software*, 31(3):397–423, 2005.
- [18] A. C. Hindmarsh, P. N. Brown, K. E. Grant, S. L. Lee, R. Serban, D. E. Shumaker, and C. S. Woodward. Sundials: Suite of nonlinear and differential/algebraic equation solvers. *ACM Transactions on Mathematical Software*, 31(3):363–396, 2005.
- [19] T.J.R. Hughes and A. Brooks. A multidimensional upwind scheme with no crosswind diffusion. *Finite element methods for convection dominated flows*, 34:19–35, 1979.
- [20] Carl-Erik Janson. *Potential Flow Panel Methods for the Calculation of Free-surface Flows with Lift*. PhD thesis, Chalmers University of Technology Gothenburg, 1997.
- [21] Carl-Erik Janson. Linear and non-linear potential-flow calculations of free-surface waves with lift and induced drag. *Proceedings of the Institution of Mechanical Engineers, Part C: Journal of Mechanical Engineering Science*, 214(6):801–812, 2000.
- [22] DW Kelly, D.S.R. Gago, OC Zienkiewicz, and I. Babuska. A posteriori error analysis and adaptive processes in the finite element method: Part I–error analysis. *International Journal for Numerical Methods in Engineering*, 19(11):1593–1619, 1983.

- [23] Martin Kjellberg. *Fully Nonlinear Unsteady Three-Dimensional Boundary Element Method for Ship Motions in Waves*. PhD thesis, Chalmers University of Technology Gothenburg, 2013.
- [24] Martin Kjellberg, Carl-Erik Janson, and Giorgio Contento. Nested Domains Technique For a Fully-Nonlinear Unsteady Three-Dimensional Boundary Element Method For Free-Surface Flows With Forward Speed. volume All Days of *International Ocean and Polar Engineering Conference*, 06 2011. ISOPE-I-11-495.
- [25] Martin Kronbichler, Timo Heister, and Wolfgang Bangerth. High accuracy mantle convection simulation through modern numerical methods. *Geophysical Journal International*, 191(1):12–29, 2012.
- [26] Michael Selwyn Longuet-Higgins and E. D. Cokelet. The deformation of steep surface waves on water - I. A numerical method of computation. *Proceedings Royal Society London*, 350(1660):1–26, 07 1976.
- [27] Q. Ma and S. Yan. Quasi ale finite element method for nonlinear water waves. *Journal of Computational Physics*, 212(1):52 – 72, February 2006.
- [28] A Mola, L Heltai, and A DeSimone. A fully nonlinear potential model for ship hydrodynamics directly interfaced with CAD data structures. In *24th International Ocean and Polar Engineering Conference*, 2014.
- [29] Andrea Mola, Luca Heltai, and Antonio De Simone. Ship Sinkage and Trim Predictions Based on a CAD Interfaced Fully Nonlinear Potential Model. volume All Days of *International Ocean and Polar Engineering Conference*, 06 2016. ISOPE-I-16-438.
- [30] Andrea Mola, Luca Heltai, and Antonio DeSimone. A stable and adaptive semi-Lagrangian potential model for unsteady and nonlinear ship-wave interactions. *Eng. Anal. Bound. Elem.*, 37(1):128–143, January 2013.
- [31] Andrea Mola, Luca Heltai, and Antonio DeSimone. Wet and dry transom stern treatment for fully nonlinear potential flow simulations of naval hydrodynamics. *Journal of Ship Research*, 61(1):1–14, 2017.
- [32] S. E. Mousavi and N. Sukumar. Generalized Duffy transformation for integrating vertex singularities. *Computational Mechanics*, 45(2-3):127–140, 2010.
- [33] Alfio Quarteroni and Luca Formaggia. Mathematical modelling and numerical simulation of the cardiovascular system. In *Computational Models for the Human Body*, volume 12 of *Handbook of Numerical Analysis*, pages 3–127. Elsevier, 2004.

- [34] Hoyte C. Raven. *A solution method for the nonlinear ship wave resistance problem*. PhD thesis, Technische Universiteit Delft, 1998.
- [35] James Reinders. *Intel Threading Building Blocks: Outfitting C++ for Multi-core Processor Parallelism*. O'Reilly \& Associates, Inc., first edition, 2007.
- [36] Filippo Guido Davide Sacco. A 3d adaptive boundary element method for potential flow with nonlinear kutta condition. Master's thesis, Mathematics Department, Politecnico di Milano, 2017.
- [37] S.M. Scorpio. *Fully Nonlinear Ship-Wave Computations Using a Desingularized Method*. PhD thesis, Department of Naval Architecture and Marine Engineering, University of Michigan, 1997.
- [38] David C Scullen. *Accurate Computation of Steady Nonlinear Free-Surface Flows*. PhD thesis, University of Adelaide, 1998.
- [39] J C F Telles. A Self-Adaptive Co-ordinate Transformation For Efficient Numerical Evaluation of General Boundary Element Integrals. *International Journal for Numerical Methods in Engineering*, 24:959–973, 1987.
- [40] T.E. Tezduyar. Computation of moving boundaries and interfaces and stabilization parameters. *International Journal for Numerical Methods in Fluids*, 43(5):555–575, 2003.